Epithelial–Mesenchymal Transition Shapes the Lipotoxic Response of Colon Cancer Cells to Palmitic Acid

Authors

Francesco Vari, Ilaria Serra, Elisa Bisconti, Eleonora Stanca, Antonella Raffo-Romero, Sarah Mehenni, Yanis Zirem, Daniele Vergara, Isabelle Fournier, Anna Maria Giudetti, and Michel Salzet

Correspondence

isabelle.fournier@univ-lille.fr;
anna.giudetti@unisalento.it;
michel.salzet@univ-lille.fr

In Brief Statement

Epithelial–mesenchymal transition (EMT) profoundly rewires the proteomic networks that control lipid handling, lipid droplet biogenesis, and mitochondrial resilience in colorectal cancer cells. Using epithelial-like HCT15 and mesenchymal-like HCT116 cells, integrated quantitative proteomics and metabolic profiling reveal that EMT status modulates lipotoxic outcomes. These results indicate that, in response to palmitic acid, cells either undergo cell death or adapt by increasing lipid storage and enhancing their metabolic flexibility. This work identifies EMT-driven lipid remodeling as a possible determinant of lipotoxic stress responses.

Graphical Abstract

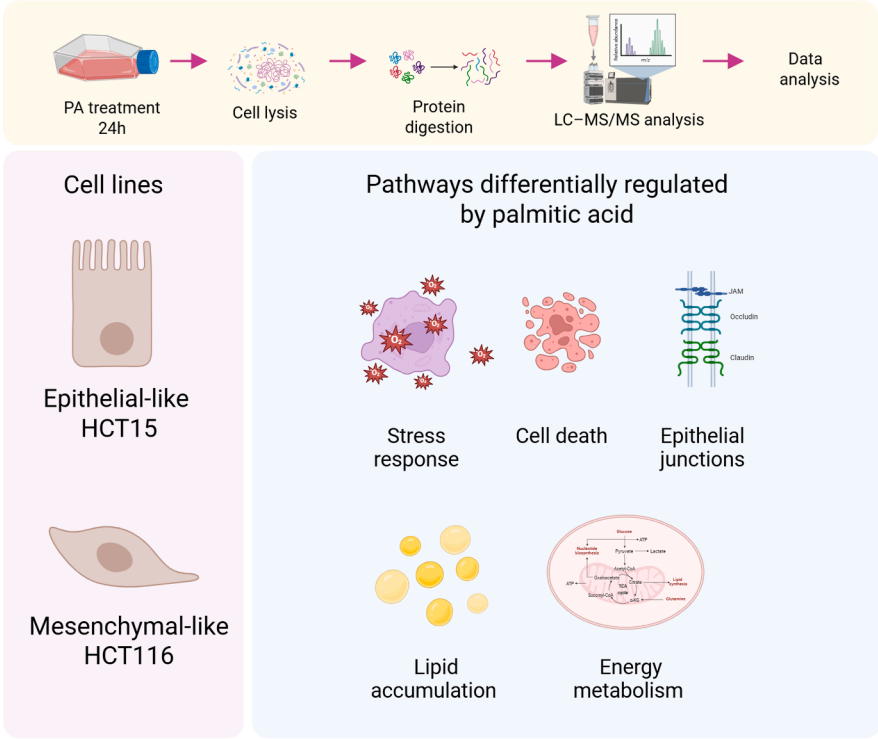

Highlights

- Proteomics reveals divergent lipid storage and metabolic programs in CRC cells.
- EMT-driven proteomics modulates cellular sensitivity to palmitic acid stress.
- Mesenchymal-like cells show stronger lipid storage and resistance to lipotoxicity.

2026, Mol Cell Proteomics *25*(*4*), 101554

https://doi.org/10.1016/j.mcpro.2026.101554

Epithelial–Mesenchymal Transition Shapes the Lipotoxic Response of Colon Cancer Cells to Palmitic Acid

Francesco Vari[1,2,‡], Ilaria Serra[1,2,‡], Elisa Bisconti[2], Eleonora Stanca[2], Antonella Raffo-Romero[3], Sarah Mehenni[3], Yanis Zirem[3], Daniele Vergara[2], Isabelle Fournier[3,*], Anna Maria Giudetti[2,*], and Michel Salzet[3,*]

Saturated fatty acids such as palmitic acid (PA) can induce lipotoxic stress, whereas monounsaturated fatty acids like oleic acid (OA) often promote adaptive responses through lipid droplets (LDs) formation. Here, we reveal that epithelial–mesenchymal transition (EMT) profoundly influences the lipotoxic response of colorectal cancer cells. Using the epithelial-like HCT15 and mesenchymal-like HCT116 cell lines, we combined proteomic, metabolic, and imaging analyses to elucidate how EMT status determines lipid storage capacity and resistance to PA-induced toxicity. A basal proteomic profiling highlighted a striking divergence in metabolic changes: HCT15 cells displayed enhanced glycolysis and reduced expression of LDs biogenesis proteins, while HCT116 cells exhibited oxidative metabolism and a "lipid-rich" proteomic signature enriched in PLIN2, GPAT3, and DGAT1. Functionally, PA triggered massive cytotoxicity and failed to induce LDs in HCT15 cells, correlating with DGAT1/2 downregulation and suppressed triacylglycerol synthesis. In contrast, HCT116 cells showed modest LDs accumulation, preserved mitochondrial function, and strong resistance to lipotoxic stress. OA treatment restored LDs formation and cell viability in both models, underscoring the protective role of unsaturated fatty acids. Notably, forced EMT induction in HCT15 cells by PMA markedly enhanced LDs accumulation and reduced PA-induced death, confirming that EMT confers metabolic plasticity and lipid-buffering capacity. These findings demonstrate that EMT status modulates differential lipid handling and stress adaptation in colon cancer cells, linking mesenchymal transition to enhanced LDs biogenesis and survival under lipotoxic conditions. Data are available via ProteomeXchange with identifier PXD071641.

INTRODUCTION

The colon, or large intestine, is a pivotal component of the digestive tract, primarily responsible for absorbing nutrients, water, electrolytes, and vitamins from the intestinal lumen (1). The epithelial cells lining the colon form a continuous layer connected by tight junctions (TJs) between neighboring epithelial cells, which are crucial for maintaining the integrity of the intestinal barrier (2).

E-cadherin (E-cad), a calcium-dependent adhesion molecule, is prominently located at these junctions. Functional cell adhesion relies on the interaction between E-cad and cytoplasmic proteins known as catenins (3). Specifically, β-catenin (β-cat) binds to the cytoplasmic domain of E-cad, linking it to the actin cytoskeleton, thereby contributing to tissue integrity and robust cell-cell adhesion (4, 5).

Disruption of this epithelial integrity is a hallmark of the epithelial-mesenchymal transition (EMT), a dynamic process through which epithelial cells lose polarity and adhesion, acquiring mesenchymal features such as increased motility and invasiveness. EMT plays a critical role not only in development and wound healing but also in cancer progression, where it enhances metastatic potential and confers resistance to various stressors, including nutrient overload and lipotoxicity (6).

The intestinal barrier is extremely sensitive to dietary influences, with certain components capable of inducing dysfunction. A shift from traditional to a Western diet, particularly rich in saturated fats, can compromise membrane integrity, leading to gastrointestinal disorders and triggering local and systemic inflammation (7). Under high-fat dietary conditions, enzymes known as diacylglycerol

From the [1]Department of Physiology and Pharmacology "V. Erspamer", Sapienza University of Rome, Rome, Italy; [2]Department of Biological and Environmental Sciences and Technologies (DiSTeBA), University of Salento, Lecce, Italy; [3]University of Lille, Inserm, CHU Lille, U-1192 - Laboratoire Protéomique Réponse Inflammatoire Spectrométrie de Masse - PRISM, Lille, France

[‡]These authors equally contributed to the work

*For correspondence: Anna Maria Giudetti, anna.giudetti@unisalento.it; Isabelle Fournier, isabelle.fournier@univ-lille.fr; Michel Salzet, michel.salzet@univ-lille.fr.

https://doi.org/10.1016/j.mcpro.2026.101554

O-acyltransferases (DGAT1 and DGAT2) play a crucial role in lipid metabolism. These enzymes catalyze the final step of triacylglycerol (TAG) synthesis, converting diacylglycerol and acyl-CoA into TAG. Intestinal DGAT1 is essential for dietary fat absorption and storage. In response to a high-fat diet (HFD), DGAT1 activity is upregulated, facilitating the conversion of excess diacylglycerols into TAG, which helps regulate lipid levels within intestinal cells and prevents the toxic accumulation of free fatty acids (FFAs) (8). DGAT2 also contributes to lipid accumulation in intestinal cells by supporting TAG synthesis, especially when dietary fat intake is elevated.

Nutrient overload can induce endoplasmic reticulum (ER) stress, triggering the unfolded protein response (UPR), which governs the autophagy pathway, crucial for lipid metabolism (9). The effects of ER stress and autophagy can vary by tissue. Recently, we demonstrated a differential regulation of DGAT1 and DGAT2 under lipotoxicity induced by palmitic acid (PA) in hepatic cancer cell lines (10).

PA, a saturated fatty acid, and oleic acid (OA), a monounsaturated fatty acid, are the most abundant fatty acids in the diet and plasma, representing 31% and 27% of total plasma non-esterified fatty acids, respectively (11). These fatty acids exert distinct effects on cellular metabolism. PA is often associated with pro-inflammatory responses and has been implicated in promoting cancer cell proliferation and survival (12). In contrast, OA has been linked to anti-inflammatory effects and may inhibit cancer cell growth through various mechanisms, including the modulation of signaling pathways related to apoptosis and cell cycle regulation (13, 14). Research has shown that PA can impair intestinal barrier integrity and induce inflammation by disrupting paracellular permeability and altering TJ expression and localization (15).

Beyond classical apoptotic and necrotic mechanisms, ferroptosis has recently emerged as a distinct form of regulated cell death characterized by the accumulation of lipid peroxides derived from polyunsaturated fatty acids and critically dependent on enzymes such as acyl-CoA synthetase long chain family member 4 (ACSL4) and iron metabolism pathways (16). Several studies have shown that saturated fatty acids, including PA, can create conditions that favor ferroptosis, especially in cells with impaired lipid droplets (LDs) formation and reduced capacity to neutralize toxic lipid intermediates. In this context, comparing epithelial- and mesenchymal-like intestinal cells may provide novel insights into the relationship between lipotoxicity, EMT, and vulnerability to ferroptosis (17).

This study aims to compare the effects of PA and OA on two human colon cancer cell lines, HCT15 and HCT116, which exhibit distinct cellular characteristics. HCT116 cells display a mesenchymal-like phenotype, characterized by increased migratory and invasive capabilities, reduced E-cad expression, and alterations in cell adhesion properties (18). Conversely, HCT15 cells retain epithelial traits, including stronger cell-cell adhesion and lower motility, potentially rendering them more susceptible to lipid-induced stress and membrane dysfunction (19). From a genomic perspective, HCT116 cells are *TP53* wild-type, whereas HCT15 cells harbor a *TP53* loss-of-function mutation, a distinction that may also affect their metabolic responses (20). We found that HCT15 and HCT116 respond differently to PA treatment, regarding both lipotoxicity and LDs accumulation. Proteomic analysis showed distinct differences between the 2 cell lines that align with their EMT phenotypes. Moreover, the EMT transition was able to partially reverse these differences, further supporting the idea that EMT underlies the divergent cellular behaviors observed in HCT15 and HCT116. Together, these results underscore the importance of EMT in shaping lipotoxic responses and highlight the potential of EMT-targeting strategies for modulating metabolic stress associated with fatty acid overload.

MATERIALS AND METHODS

Cell Treatments and Reagents

HCT15 and HCT116 human colon cancer cell lines were maintained in Dulbecco's Modified Eagle Medium (DMEM, Sigma-Aldrich D5546) low glucose with 10% fetal bovine serum (FBS, Capricorn HI-12A), 100 U/ml penicillin, 100 μg/ml streptomycin (Sigma-Aldrich #P4333), and 2 mM glutamine (Sigma-Aldrich G7513). Cells were cultured at 37 °C with 5% partial pressure of CO2 in a humidified atmosphere. Both cell lines were regularly tested for *mycoplasma* contamination using a *Mycoplasma* Detection Kit (Aurogene, REP-MYSNC-100). OA (COD. 75090), PA (COD. 506345), and bovine serum albumin (BSA), fraction V fatty acid-free (COD. 03117057001) were purchased from Merck. Fatty acids were dissolved in fatty-acid-free BSA at 8 mM concentration and were subsequently diluted to the desired final concentration in DMEM immediately before cell treatments. To mimic physiological albumin-bound FFA delivery and to maintain fatty acid solubility, PA and OA were prepared as fatty acid-BSA complexes (8 mM stock in 10% (w/v) fatty-acid-free BSA) and diluted into culture medium. Vehicle control cells were treated with fatty-acid-free BSA alone at the same final concentration as in the fatty acid-BSA solutions (final BSA ~0.25% (w/v)). The PA/OA treatment media, therefore, contained BSA, which is required to prevent precipitation and to approximate physiological fatty acid transport by serum albumin (21, 22). For cell treatments with PA and OA, we chose the concentration of 0.2 mM, which represents the physiological postprandial intestinal concentration, and is within the concentration range of FFAs in human plasma (i.e., 0.2–2 mM) (22, 23). For EMT induction, colon cancer cells were plated onto a 6-well plate for 24 h. Cells were then treated in triplicate with 100 nM Phorbol 12-myristate 13-acetate (PMA, Santa Cruz sc-3576) for 24 h before being subjected to PA treatment for an additional 24 h. For autophagy inhibition of colon cancer cells, 100 μM of chloroquine (Cell signaling #14774) was added 4 h before the incubation ending.

Cell Viability Assay

Cell viability was evaluated using the crystal violet assay on adherent cells. Cells were seeded in a 96-well plate at a density of 10,000 cells per well. After treatment, cells were washed with phosphate-buffered saline (PBS) and fixed with 4% paraformaldehyde (PFA) for 30 min at room temperature. The cells were

then stained with 0.1% crystal violet (Sigma Aldrich, Cat. no. C0775) solution for 1 h at room temperature. The stain was removed through multiple washes with distilled water until the solution was clear. The plate was left to air dry. To solubilize the crystal violet, 100% ethanol was added, and the absorbance of the dye was measured at 550 nm.

Analysis of Proteomics Data

Whole-cell lysates from colorectal cancer cell lines HCT15 and HCT116, treated with PA or with BSA as a vehicle control, were subjected to label-free quantitative proteomic analysis.

Sample preparation and digestion. proteins were extracted using a lysis buffer supplemented with protease and phosphatase inhibitors. Protein concentrations were determined using the bicinchoninic acid (BCA) assay and 50 μg of protein per sample were processed. Samples were reduced, alkylated and digested overnight at 37 °C using a filter-aided sample preparation (FASP) workflow on Amicon Ultra-0.5 ml centrifugal filters (30 kDa MWCO; Millipore). After digestion, peptides were acidified by adding trifluoroacetic acid (TFA) to a final concentration of 5% (v/v) to quench proteolysis. NaCl was added to a final concentration of 50 mM and samples were incubated for 10 min at room temperature to promote precipitation of remaining interfering substances. After centrifugation (14,000×*g*, 15 min), the peptide-containing supernatant was recovered, dried and reconstituted in 60 μl of 0.1% formic acid (FA). A volume of 20 μl from each sample was desalted using an Evotip Pure (Evosep, Denmark) according to the manufacturer's protocol.

LC–MS/MS acquisition (DIA-PASEF). Peptides were analyzed using an Evosep One liquid chromatography (LC) system coupled to a timsTOF HT mass spectrometer (Bruker Daltonics). The LC system operated under the 60 samples-per-day (60 SPD) method using a C18 performance column (EV1109; 8 cm × 150 μm, 1.5 μm particle size) maintained at 40 °C and connected to a fused silica emitter (10 μm i.d., Bruker) integrated into a CaptiveSpray ion source. Mobile phases were 0.1% FA in water (A) and 0.1% FA in acetonitrile (B). Data were acquired in diaPASEF mode. MS1 survey scans were recorded over an m/z range of 100 to 1700 and an ion mobility range of $1/K_0$ = 0.6 to 1.6 V s/cm^2. For fragmentation analysis, the precursor m/z range was fractionated in the quadrupole/ion-mobility plane using 24 diagonal diaPASEF isolation windows (3 × 8 windows) of 25 m/z width each spanning m/z 400 to 1000 across the full ion mobility range ($1/K_0$ = 0.6–1.6 V s/cm^2). No window overlap was applied. The ramp/accumulation time was 100 ms, resulting in a total cycle time of ~1.2 s. Collision energy was linearly ramped as a function of ion mobility (approximately 20–59 eV).

DIA data processing, identification criteria, and quantification. Raw diaPASEF data were processed with DIA-NN (version 2.1) for peptide identification and protein quantification (Demichev *et al*., Nat Methods 2020). A project-specific spectral library was generated in DIA-NN using the library-free (directDIA) workflow. Searches were performed against the UniProt *Homo sapiens* reference proteome (release 2024_12; downloaded December 2024; ~82,000 protein entries), supplemented with common contaminants. Enzyme specificity was set to trypsin/P with up to two missed cleavages. Carbamidomethylation of cysteine was set as a fixed modification; methionine oxidation and protein N-terminal acetylation were set as variable modifications. Precursor and fragment ion mass tolerances were set to 20 ppm. Identifications were accepted at 1% false discovery rate (FDR) at both precursor and protein-group levels using DIA-NN's target-decoy strategy. Protein quantification was performed using MS2 fragment-ion intensities with DIA-NN interference correction enabled and cross-run normalization activated (robust LC mode).

Downstream statistical analysis and visualization. DIA-NN output tables were imported into Perseus (version 1.6.10.43). Protein intensities were $\log_2$-transformed and normalized before analysis. Proteins identified in at least two biological replicates per condition were retained. Missing values were imputed using a low-abundance normal distribution. Differential expression was assessed by two-sample *t* test with Benjamini–Hochberg correction for multiple testing (FDR <0.05); unadjusted *p*-values are additionally reported for exploratory comparisons. Venn diagrams illustrating protein overlap and uniqueness between the 2 cell lines were generated using InteractiVenn (24). Additional analyses were performed using Profiler (25) for functional enrichment and STRING for interactome analysis (26).

Analysis of Cellular Bioenergetic Profiles Using Seahorse XFp

For bioenergetic studies, 10.000 cells/well were seeded in the XFp cell culture miniplates. The results were normalized to the total cell number following DAPI staining. Each Oxygen consumption rate (OCR)/extracellular acidification rate (ECAR) measurement cycle consisted of 3 min mixing, 2 min waiting and 3 min measurement, repeated three times for each assay step, following the manufacturer's recommendations. Each condition was measured using 4 to 6 technical replicate wells per experiment, and experiments were repeated in at least three independent biological replicates. The assay was executed in XF DMEM Medium pH 7.4 media (Agilent, Santa Clara, California, United States; Cat. #103575-100) containing 5.5 mM glucose (Agilent, Cat. #103577-100), 2 mM L-glutamine (Agilent, Cat. #103579-100) and 1 mM sodium pyruvate (Agilent, Cat. #103578-100). Next, cells were incubated at 37 °C in a non-CO2 incubator for 1 h. OCR and ECAR were measured under basal conditions and in response to sequentially injected compounds at a final concentration of 1.5 μM oligomycin (Sigma-Aldrich Cat. #O4876), 2 μM FCCP (Sigma-Aldrich Cat. #C2920), and 0.5 μM rotenone (Sigma-Aldrich Cat. #R8875) + 0.5 μM antimycin A (Sigma-Aldrich Cat. #A8674) and 50 mM of 2-deoxy-D-glucose (2-DG, Sigma-Aldrich Cat. #D6134). Stocks of compounds were prepared in the same DMEM media and loaded into the delivery ports of Seahorse cartridges. The parameters related to respiration were assessed, including non-mitochondrial respiration (OCR after rotenone-antimycin A injection), basal mitochondrial respiration (ΔOCR between the steady state and after rotenone-antimycin A injection), ATP-linked respiration (ΔOCR between basal mitochondrial respiration and after oligomycin injection), and maximal mitochondrial respiration (ΔOCR between non-mitochondrial respiration and after FCCP injection). The parameters related to glycolysis were assessed, including non-glycolytic acidification (ECAR after 2-DG injection), glycolysis (ΔECAR between the steady state and after 2-DG injection), maximal glycolytic capacity (ΔECAR between non-glycolytic acidification and after oligomycin injection), and glycolytic reserve (ΔECAR between the steady state and after oligomycin injection).

BODIPY Staining

BODIPY 493/503 staining was performed on cells cultured on coverslips (60–80% confluency) in 12-well plates. After treatment, cells were washed with PBS and incubated for 15 min at 37 °C with the dye (1:1000 dilution from a 1 mg/ml stock in PBS). Following three washes with PBS, the slides were mounted using Dako Fluorescent Mounting Medium (Agilent) and imaged with an inverted confocal microscope (Zeiss Axio Observer Z1 equipped with an LSM 780 scanning head; Zeiss). Images were acquired with ZEN Black software using the 63 × /1.4 oil-immersion objective with a 20 μm scale bar. LDs number and area were quantified using FIJI software (version 2.9.0/1.53). For each condition, three representative images were acquired using identical microscope settings. Quantification was performed using the "Analyze Particles" function, with size and circularity filters set to exclude background noise. This function

provided measurements of both the number of LDs and the total area per field of view. All data were normalized to the number of cells per image.

Thin-Layer Chromatography (TLC)

Total lipids were extracted from HCT15 and HCT116 cells using methyl-tert-butyl ether as an extraction solvent, as reported in (27). Extracted lipids were loaded on silica gel plates for thin-layer chromatography (TLC) analysis. Plates were developed with hexane/ethyl ether/acetic acid (70/30/1; *v/v/v*). After development, plates were uniformly sprayed with 10% cupric sulfate in 8% aqueous phosphoric acid, allowed to dry for 10 min at room temperature, and then placed into a 145 °C oven for 10 min, as reported in (28). Different lipid species were identified by developing specific standards under the same experimental conditions. Spot intensity was measured by densitometric analysis.

RNA Extraction and Real-Time qPCR Analyses

Total RNA was extracted from HCT15 and HCT116 cells with TRI reagent (Zymo Research, R2050-1). RNA quantification was performed using a NanoDrop One Spectrophotometer (Thermo Scientific). For cDNA synthesis, HIScript III RT SuperMix for qPCR (+gDNA wiper) kit was used (Vazyme Biotech), following the manufacturer's instructions. Gene expression analyses were performed through real-time RT-PCR using iTaq Universal Sybr Green Supermix (Bio-Rad), run on the Rotor-Gene Q 6000 System (Qiagen). A comparative analysis was performed. Glyceraldehyde-3-phosphate dehydrogenase (GAPDH) and β-actin were evaluated as housekeeping genes, resulting in stable overall samples. GAPDH was chosen as the reference gene. All predesigned primers were obtained from Bio-Rad (more information is available at www.bio-rad.com/PrimePCR). The list of primers is reported in Supplementary Table S1.

Western Blot

Proteins were extracted from cells using RIPA lysis buffer (Cell Signaling #9806). Total protein levels were determined using the Bradford method (Bio-Rad Laboratories). After boiling for 5 min, proteins were loaded and separated by SDS-polyacrylamide gel electrophoresis. The samples were then transferred onto a nitrocellulose membrane (Bio-Rad Laboratories) and blocked at room temperature for 1 h using 5% (w/v) non-fat milk in TBS-Tris buffer (Tris-buffered saline (TBS) plus 0.5% (v/v) Tween-20, TTBS). The membranes were incubated with the primary antibodies reported in Supplementary Table S2. After washing with TTBS, the blots were incubated with peroxidase-conjugated monoclonal secondary antibodies (Sigma-Aldrich) at 1:10.000 dilutions at room temperature for 1 to 2 h. The blots were then washed thoroughly in TTBS. Western blotting analyses were performed using the Amersham ECL Advance Western Blotting Detection Kit (GE Healthcare), and the ChemiDoc system (Bio-Rad) was used for chemiluminescence measurement. Densitometric analysis of the immunoblots was performed using Image LabTM Version 6.0.1 2017 (Bio-Rad Laboratories, Inc.) software.

Statistical Analysis

Results are expressed as means ± standard deviation (SD). Statistical differences for cell-based assays were evaluated using GraphPad Prism version 8.3.0 for Windows. Comparisons were performed using one-way analysis of variance (ANOVA) followed by Tukey's post hoc test, unless otherwise indicated. Differences were considered statistically significant when $p < 0.05$. For proteomic data, statistical analyses were performed in Perseus version 1.6.10.43 using the DIA-NN protein-group intensity matrix. Protein intensities were $\log_2$-transformed and normalized before analysis. Proteins quantified in at least two biological replicates per condition were retained. Missing values were imputed using a low-abundance normal distribution. Differentially expressed proteins were determined by a two-sample *t* test (six biological replicates per condition) with Benjamini-Hochberg correction for multiple testing; proteins with FDR <0.05 were considered significant. For exploratory comparisons, unadjusted *p*-values are additionally reported.

Experimental Design and Statistical Rationale

For the MS-based proteomics experiment, two colorectal cancer cell lines (HCT15 and HCT116) were analyzed under two conditions (BSA vehicle control vs PA 0.2 mM for 24 h). Each condition was analyzed using six independent biological replicates (n = 6), each originating from an independent cell culture, protein extraction and digestion. Peptide digests were injected once per biological replicate (one technical LC-MS/MS run per digest) and sample acquisition order was randomized to minimize batch effects. DIA-PASEF provides high quantitative precision and data completeness, and the use of n = 6 biological replicates enables detection of moderate effect sizes while supporting multiple-testing correction (Benjamini-Hochberg FDR) for robust identification of differentially expressed proteins. For all other cellular assays (viability, lipid droplet imaging, TLC, Seahorse, RT-qPCR and Western blotting), experiments were performed in at least three independent biological replicates, with technical replicates as described in the respective method sections.

RESULTS

Proteomic Profiling of HCT15 and HCT116 Cell Lines

We performed an unbiased, exploratory global proteomic analysis (Benjamini-Hochberg FDR <0.05; see Methods) to delineate baseline molecular differences between the colorectal cancer cell lines HCT15 and HCT116. Approximately 6.000 proteins were identified across the two models. Hierarchical clustering (Fig. 1*A*) resolved two distinct expression clusters: Cluster one comprised proteins markedly upregulated in HCT15 and downregulated in HCT116, whereas Cluster two included proteins enriched in HCT116 and suppressed in HCT15, indicating clearly segregated proteomic phenotypes. Functional enrichment analysis (Fig. 1*B*) demonstrated that HCT15 cells preferentially engage in glycolytic pathways, while HCT116 cells predominantly rely on oxidative metabolism. In Supplementary Table S3 proteins that are upregulated in HCT15 or HCT116 cells are categorized based on their functions. Consistently, LDHA and LDHB, key enzymes orchestrating the metabolic equilibrium between glycolysis and oxidative phosphorylation, were significantly upregulated in HCT15 cells compared to HCT116 cells (Supplementary Table S4). This metabolic divergence was corroborated by Seahorse flux analysis, showing elevated basal respiration in HCT116 and enhanced glycolytic activity in HCT15 (Fig. 1*C*).

Volcano plot analysis further revealed robust differential protein expression between the 2 cell lines (Fig. 1*D*). While most proteins clustered around the origin ($\log_2$ fold change ≈ 0), reflecting overall comparable expression levels, distinct subsets exhibited significant positive or negative fold

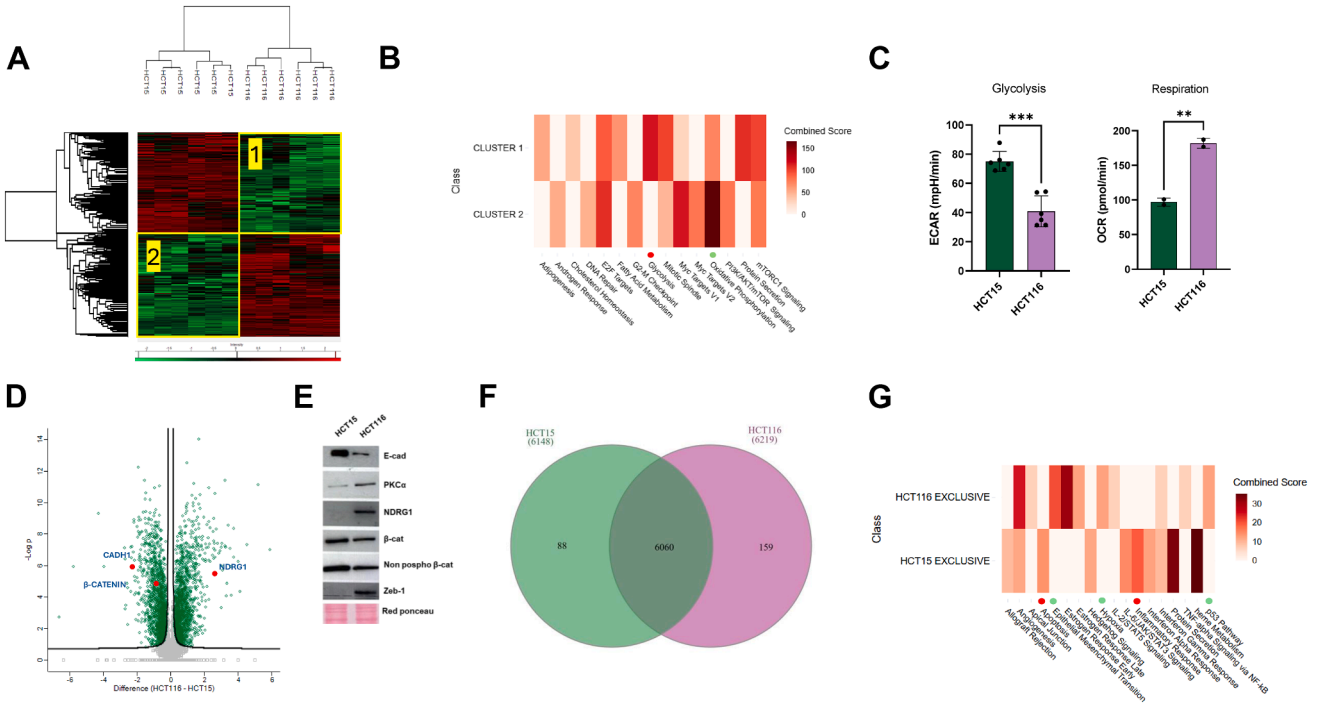

FIG. 1. **Comparative proteomic profile of HCT15 and HCT116 cells.** *A*, heatmap and hierarchical clustering of differentially expressed proteins between HCT15 and HCT116 colorectal cancer cell lines, derived from quantitative proteomic profiling. The color scale ranges from *green* (downregulated) to *red* (upregulated), with *black* indicating no variation in expression. The analysis identifies two major clusters (Cluster 1 and Cluster 2), which reflect distinct proteomic signatures between the cell lines. *B*, functional enrichment analysis of basal proteomic profiles, highlighting the most significantly enriched biological processes and signaling pathways in both cell lines. Red and green dots correspond to pathways with predominant protein contributions in HCT15 and HCT116 cells, respectively. *C*, basal metabolic phenotyping of the 2 cell lines, illustrated through oxygen consumption rate (OCR) and extracellular acidification rate (ECAR) measurements, which indicate mitochondrial respiration and glycolytic activity, respectively. *D*, volcano plot depicting differentially expressed proteins between HCT116 and HCT15 cells. The x-axis represents $\log_2$ fold-change (HCT116 vs. HCT15), while the y-axis indicates $-\log_{10}$ *p*-value. *E*, Western blot validation of selected proteins involved in cell adhesion and intracellular signaling, including E-cadherin, PKCα, NDRG1, β-catenin, non-phospho β-catenin, and ZEB1, in both cell lines. Ponceau S staining served as a total-protein loading control. *F*, venn diagram showing shared and unique proteins identified in HCT15 and HCT116 cell lines. *G*, functional enrichment analysis of cell-line-exclusive proteins, illustrating biological processes and pathways predominantly associated with proteins uniquely detected in HCT15 (*red*) or HCT116 (*green*) cells.

changes with strong statistical confidence, indicating cell line-specific regulatory signatures.

Consistent with their predominantly epithelial phenotype, HCT15 cells displayed higher levels of E-cadherin, whereas HCT116 cells showed increased Zeb-1 expression. Non-phosphorylated β-catenin, a key regulator of EMT, was also elevated in HCT15 relative to HCT116. Conversely, HCT116 cells expressed higher levels of PKCα, a known EMT inducer, together with NDRG1, a context-dependent EMT modulator. In addition, HCT15 cells exhibited increased abundance of multiple epithelial markers, supporting a more differentiated and cohesive epithelial phenotype (Supplementary Table S3 and S4). Western blot analysis of core EMT regulators corroborated our proteomic findings (Fig. 1*E*).

The Venn diagram (Fig. 1*F*) confirmed both shared and exclusive proteomic features, with 6.060 proteins common to both lines, 88 detected only in HCT15, and 159 unique to HCT116 (Supplementary Table S5 and S6). Proteins exclusive to HCT116 were enriched in pathways related to EMT, hypoxia, and p53 signaling, whereas those unique to HCT15 were predominantly associated with apoptosis and inflammatory processes (Fig. 1*G*, Supplementary Table S5 and S6). Notably, a substantial proportion of the exclusive proteins in both cell lines mapped to lipid metabolism. HCT15 lacked several proteins required for LDs biogenesis, which were instead uniquely expressed in HCT116, PLIN2, DHRS3, and reduced levels of CAV-1, GPAT3, DGAT, LDAF1, and MFN2 compared to HCT116 (Supplementary Table S3–S6). Moreover, enzymes involved in cholesterol esterification, such as ACAT1 and ACAT2, and the autophagy-associated protein ATG2A were more expressed in HCT15 than HCT116 cells. The consistency of our results with data from the Human Protein Atlas database further strengthens our observations (29). The differences between HCT15 and HCT116 cells in LDs-associated proteins suggest two distinct cell strategies. HCT116 cells display a “lipid-rich” phenotype, characterized by enhanced lipid storage that supports rapid growth,

membrane biosynthesis, and stress resistance. In contrast, HCT15 cells preferentially rely on lipid recycling and autophagy to maintain energy balance and ensure survival under metabolic stress conditions. This trait is functionally relevant, as LD formation is essential for buffering lipid-induced toxicity and maintaining metabolic homeostasis under elevated fatty acid exposure.

Palmitic Acid Differentially Induces Lipid Droplet Formation in HCT15 and HCT116 Cells

PA significantly decreased HCT15 cell viability, causing approximately 40% and 80% cell death at 24 and 48 h, respectively, as determined by crystal violet staining (Supplementary Fig. S1*A*). Conversely, HCT116 cells were remarkably resistant to PA, exhibiting only ~20% loss of viability at 48 h (Supplementary Fig. S1*B*). Based on the proteomic results, we sought to further investigate the metabolism of LDs in the 2 cell lines. We selected PA, a saturated fatty acid classically associated with lipotoxic stress, and OA, a monounsaturated fatty acid known to counteract PA-induced toxicity and promote neutral lipid storage. This approach enabled us to examine how fatty acid composition modulates cell viability and lipid accumulation.

Bright-field microscopy showed that PA exposure markedly altered HCT15 cell morphology, inducing pronounced cell shrinkage, rounding, detachment, and a clear reduction in cell density (Supplementary Fig. S1*C*). Co-treatment with OA partially restored cell morphology and confluence, indicating a protective effect of OA against PA-induced cytotoxicity. In stark contrast, HCT116 cells displayed minimal morphological changes upon PA treatment, maintaining normal morphology and adherence without substantial loss of confluence or evident cell death under any condition (Supplementary Fig. S1*D*).

Consistent with these observations, together, these results demonstrate a marked cell line-specific sensitivity to saturated fatty acid exposure, with HCT116 cells being substantially more resistant to PA-induced cytotoxicity than HCT15 cells.

Fluorescence microscopy further revealed robust LD accumulation in both cell lines following OA treatment compared to BSA (Fig. 2, *A* and *D*). OA-derived LDs were

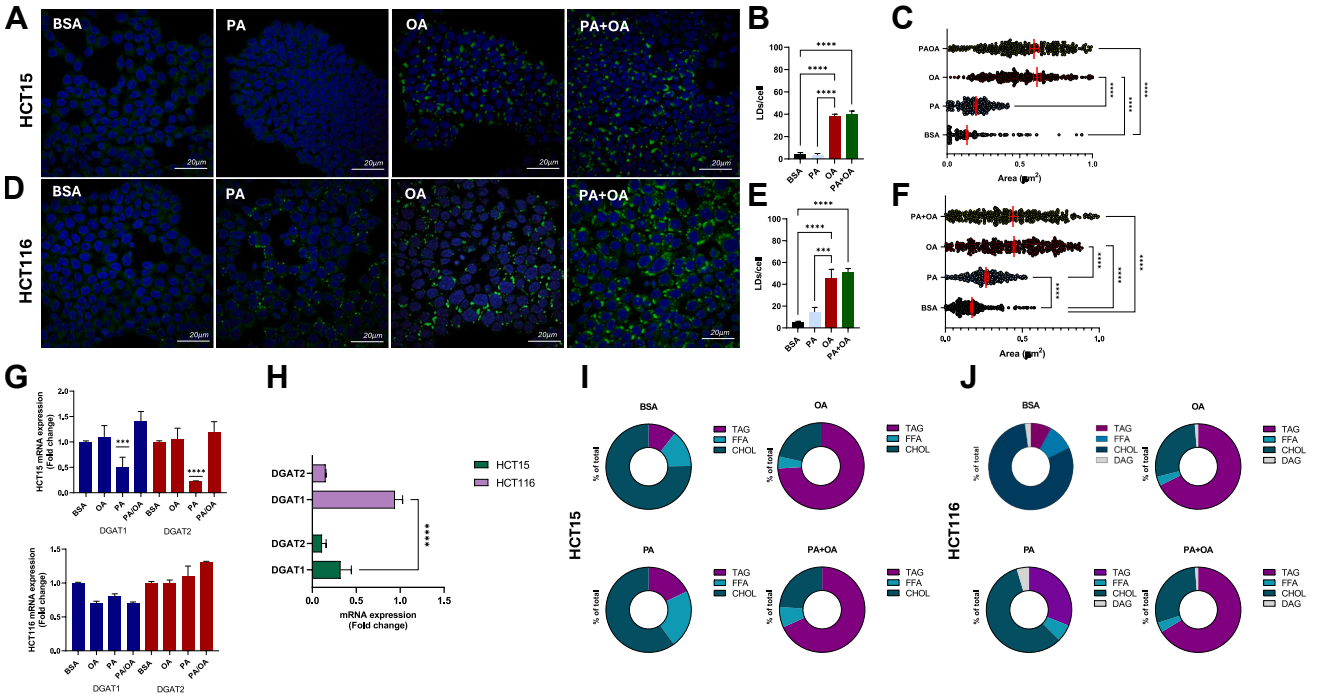

FIG. 2. **Lipid droplet metabolism in HCT15 and HCT116 cells.** Representative confocal microscopy images showing lipid droplets (LDs, *green*; stained with BODIPY) and nuclei (*blue*; stained with DAPI) in HCT15 (*A*) and HCT116 (*D*) cells treated for 24 h with BSA (control), palmitic acid (PA, 200 μM), oleic acid (OA, 200 μM), or their combination (PA + OA, 1:1 ratio, 200 μM each). Scale bar: 20 μm. Quantification of LD number per cell in HCT15 (*B*) and HCT116 (*E*), and LD area (μm^2) in HCT15 (*C*) and HCT116 (*F*) under the indicated conditions. *G*, relative mRNA expression levels of DGAT1 and DGAT2 in HCT15 and HCT116 cells, as determined by qRT-PCR. Data are expressed as fold change versus BSA. *H*, basal DGAT1 and DGAT2 expression comparison between HCT15 and HCT116. (*I*, *J*) Thin-layer chromatography (TLC) analysis of intracellular neutral lipids, including triacylglycerols (TAG), free fatty acids (FFA), cholesterol (Chol), and diacylglycerols (DAG), and their relative quantification by densitometric analysis in (*I*) HCT15 and (*J*) HCT116 cells after 24 h of treatment. Each lipid species is expressed as a percentage of the total neutral lipid content and normalized to the control group (BSA). Data represent the mean ± SD of three independent experiments. (**$p < 0.01$; ***$p < 0.001$; ****$p < 0.0001$ versus BSA).

significantly larger in HCT15 than in HCT116 cells (Fig. 2, *E* and *F*). HCT15 cells failed to accumulate appreciable LDs in response to PA alone (Fig. 2, *A* and *D*), whereas HCT116 cells formed modest LDs under PA treatment (Fig. 2, *B* and *E*), albeit fewer and smaller than those induced by OA (Fig. 2, *E* and *F*). Co-treatment with PA and OA promoted LD formation to levels comparable to OA alone in both cell lines, indicating a dominant effect of OA on lipid storage (Fig. 2, *A–F*).

Expression analysis of the TAG-synthesizing enzymes DGAT1 and DGAT2 revealed further differences between the cell lines. In HCT15 cells, PA significantly downregulated DGAT1 and DGAT2 mRNA levels, with partial rescue by OA co-treatment (Fig. 2*G*). In contrast, PA treatment did not significantly alter DGAT1 or DGAT2 expression in HCT116 cells relative to BSA. Notably, basal DGAT1 expression was substantially higher in HCT116 than in HCT15 cells (Fig. 1*H*), in agreement with our proteomic data and with The Human Protein Atlas (29), potentially contributing to the enhanced lipid storage capacity of HCT116 cells. To corroborate these findings, total lipids were extracted after 24 h of FA treatment and analyzed by TLC (Fig. 2, *I* and *J* and supplementary Fig. S2). OA induced a significant increase in TAG content in both cell lines relative to controls. Notably, PA treatment led to ~38% TAG accumulation in HCT116 cells but less than 15% in HCT15 cells (Fig. 3, *A* and *B*). As expected, PA/OA co-treatment increased TAG levels, consistent with the microscope analysis of LDs accumulation (Fig. 1*A*).

Palmitic Acid Shapes the Proteomic Landscape of HCT15 and HCT116 Colon Cancer Cells

We performed a proteomic analysis on HCT15 and HCT116 cells after PA treatment for 24 h. Hierarchical clustering of proteomic data revealed two major clusters for both cell lines. In HCT15 cells Cluster two comprised proteins upregulated by PA, while Cluster one included proteins downregulated by PA (Fig. 3*A*). In HCT116 cells, Cluster two contained proteins downregulated by PA, whereas Cluster 1 comprised proteins upregulated by PA (Fig. 3*B*). Functional enrichment analysis, performed with Profiler (based on combined score and gene count) using MSigDB_HALLMARK_2020 database, shows that PA treatment in HCT15 cells primarily upregulated proteins involved in apoptosis, fatty acid metabolism, UV response, xenobiotic metabolism, and mTORC1 signaling (Fig. 3*C*) (25). By contrast, in HCT116

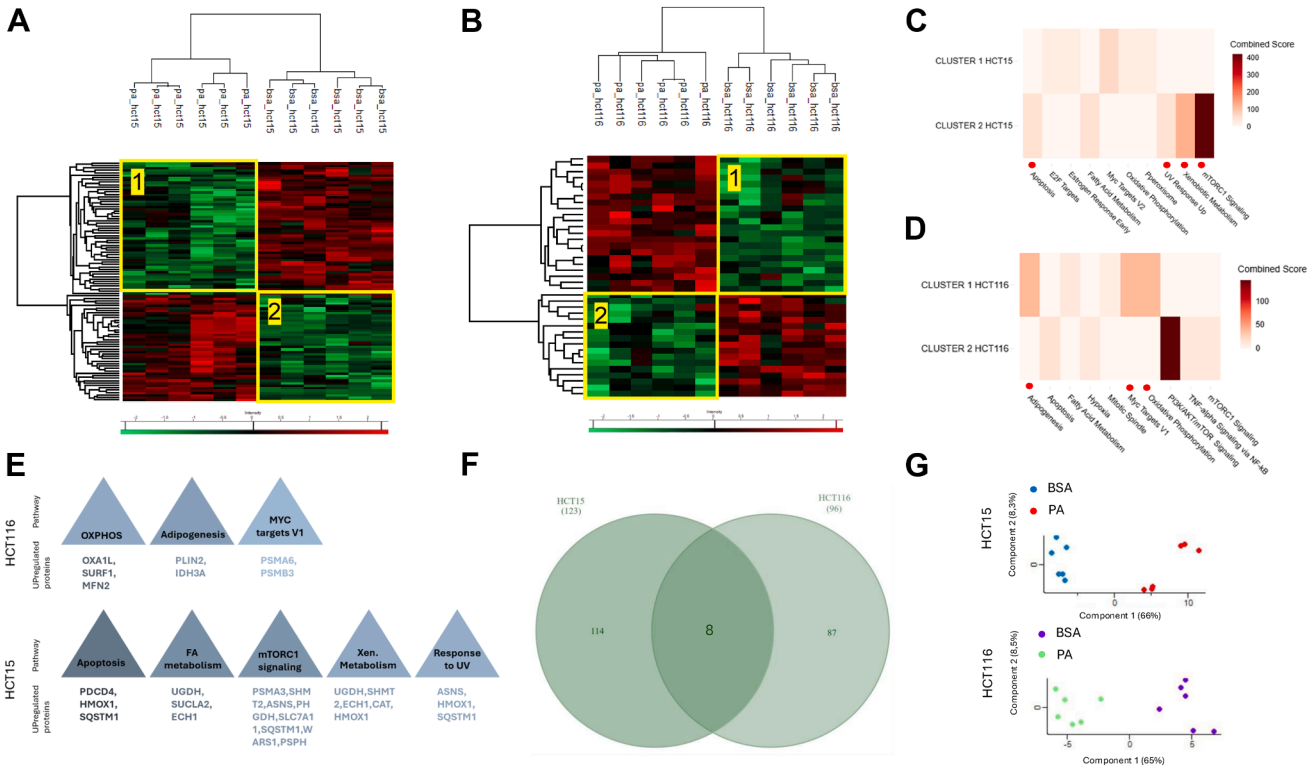

FIG. 3. **Proteomic analysis of HCT15 and HCT116 cells following palmitic acid treatment.** Heatmap representation of proteomic profiles in (*A*) HCT15 and (*B*) HCT116 cells after treatment with PA (200 μM, 24 h). Cluster two includes proteins upregulated in HCT15, whereas cluster one comprises proteins upregulated in HCT116 in response to PA. Functional enrichment analyses of upregulated proteins in (*C*) HCT15 and (*D*) HCT116 cells highlight enriched biological processes and pathways, with the most significantly affected ones shown in *red*. *E*, enrichment analysis of representative upregulated proteins belonging to major functional categories. *F*, venn diagram showing shared and unique subsets of significantly upregulated proteins ($p < 0.005$) in HCT15 and HCT116 cells following PA treatment. *G*, principal component analysis (PCA) illustrating the distribution of biological replicates and overall proteomic variance between treatments and cell lines.

cells, the upregulated proteins were mainly associated with adipogenesis, oxidative phosphorylation, and MYC target gene sets V1 (Fig. 3*D*). The proteins driving these pathways are listed and grouped by cell line and functional category (Fig. 3*E*). These findings suggest that HCT15 cells respond to PA by activating multiple stress-related programs, including apoptotic signaling, metabolic adaptation, and xenobiotic defense, indicating a higher sensitivity to lipid-induced stress. In contrast, HCT116 cells appear to reprogram their metabolism toward energy production and lipid accumulation.

The Venn diagrams comparing upregulated proteins in the 2 cell lines following PA exposure reveal eight shared proteins (GLB1L2, HMOX1, LMAN2, FAR1, SQSTM1, PNPLA2, REEP4, and TRAPPC3), probably involved in common adaptive responses to the treatment (Fig. 3*F*, Supplementary Table S7). Moreover, proteins upregulated by PA exclusively in HCT15 or HCT116 cells were 114 and 87, respectively (Fig. 3*F*). Among up-regulated proteins in HCT116 cells after PA treatment, we found PLIN2 (Supplementary Table S7), a central regulator of LD biogenesis and stabilization (30).

PCA of normalized proteomic data ($p < 0.01$) was performed to assess both treatment-induced differences and replicate homogeneity (Fig. 3*G*). In HCT15 cells, PC1 (66%) and PC2 (8%) clearly separate BSA- and PA-treated cells. A similar pattern of separation was observed in HCT116 cells (PC1 = 65% and PC2 = 8.25%). Since PC1 captures the largest source of variability, its separation of the groups indicates that the dominant difference in the dataset is driven by the effect of PA treatment, whereas PC2 accounts for a smaller portion of variability, likely reflecting secondary or subtle differences.

Transcription factors involved in the upregulation of proteins by PA were obtained by enrichment analysis using ChEA3, followed by interaction validation with STRING (Supplementary Fig. S3). In HCT15 cells, the top-ranked transcriptional factors up-regulated by PA are proteins involved in cellular responses to ER stress: CEBPG, NCOA1, GLMP, ZBED3, ATF5, NR1H4, ZNF335, DDIT3, and ZNF852. STRING analysis highlighted that ATF5, CEBPG, and DDIT3 show significant interactions with the upregulated proteins, suggesting a central role in mediating the cellular response of HCT15 to PA. In HCT116 cells, the top-ranked transcription factors XBP1, ATMIN, ZNF761, MSANTD1, THAP7, ZNF653, ESR1, ZNF883, TIGD5, and GTF2B. Notably, ESR1 and GTF2B were found to interact with key proteins of lipid metabolism, including PLIN2 and CPT1A, both upregulated by PA treatment of HCT116 cells.

The Proteomic Profile of HCT15 cells Indicates That Palmitic Acid Activates a Specific Cell Death Pathway

Building on the proteomic evidence revealing a distinct pro-apoptotic signature in PA-treated HCT15 cells, we investigated, by Western blot (Fig. 4*A*) the molecular mechanisms underlying PA-induced cell death. PA treatment dramatically elevated the p-ERK/ERK ratio in HCT15 cells compared to BSA or OA in both cell lines (Fig. 4, *A–C*). This hyperactivation coincided with striking p53 stabilization and marked suppression of YAP protein expression, orchestrating a molecular switch toward cell death commitment.

Interestingly, proteomic analysis indicated a modulation of proteins associated with apoptosis, with higher expression of Bax and reduced level of antiapoptotic Bcl-2, in HCT15 compared with HCT116 cells (Supplementary Table S4). Our comprehensive analysis of cell death markers by Western blot (Fig. 4*D*) revealed a complex picture that extends beyond classical apoptosis. Bax expression, which confirmed its major expression in HCT15 cells compared to HCT116 cells, remained unchanged in HCT15 cells but was significantly reduced in HCT116 cells following PA exposure (Fig. 4, *D* and *E*). While PA treatment selectively suppressed the anti-apoptotic protein Bcl-2 in HCT15 cells and upregulated this anti-apoptotic marker in HCT116 cells (Fig. 4, *D* and *F*), suggesting fundamentally different cellular responses to saturated fatty acid stress. The activation of PARP-1 and proteolytic cleavage of caspase-7, hallmarks of apoptotic execution, were evident in PA-treated HCT15 but not HCT116 cells (Fig. 4, *D*, *G,* and *H*). Several additional observations point toward ferroptosis as a concurrent or even predominant mechanism of PA-induced cell death in HCT15 cells. Most compellingly, PA treatment upregulated ACSL4 in HCT15 cells, while downregulating it in HCT116 cells (Fig. 4*D*). In line with this, PA treatment induced a marked increase in p16 expression in HCT15 cells while decreasing this marker in HCT116 cells (Fig. 4, *D* and *J*), further supporting a cell line-specific stress response consistent with ferroptosis vulnerability. Concomitantly, PA downregulated GPx4 expression in HCT15 but not in HCT116 cells (Fig. 4, *D* and *K*). Given that, GPx4 represents the central defense against ferroptosis by neutralizing lipid peroxides (31), its suppression coupled with ACSL4 elevation creates a molecular environment primed for ferroptosis cell death. Proteomic analysis in PA-treated HCT15 cells confirms significant upregulation of multiple ferroptosis-related proteins, including SLC7A11, HMOX1, SESN2, SQSTM1/p62, and CAT (Supplementary Table S7).

Beyond its cytotoxic effects, PA exposure triggered a profound disintegration of epithelial architecture in HCT15 cells, marked by a striking downregulation of essential junctional proteins, including E-cadherin, β-catenin, and ZO-1, at both protein and transcript levels (Fig. 4, *M–O*). Such a collapse of intercellular adhesion is a hallmark of epithelial destabilization and has been strongly associated with cancer aggressiveness and metastatic potential (32, 33). Remarkably, co-treatment with OA largely rescued this phenotype, reinstating the expression of junctional proteins and safeguarding epithelial cohesion (Fig. 4, *L–N*). In contrast, HCT116 cells exhibited a striking resistance to PA challenge,

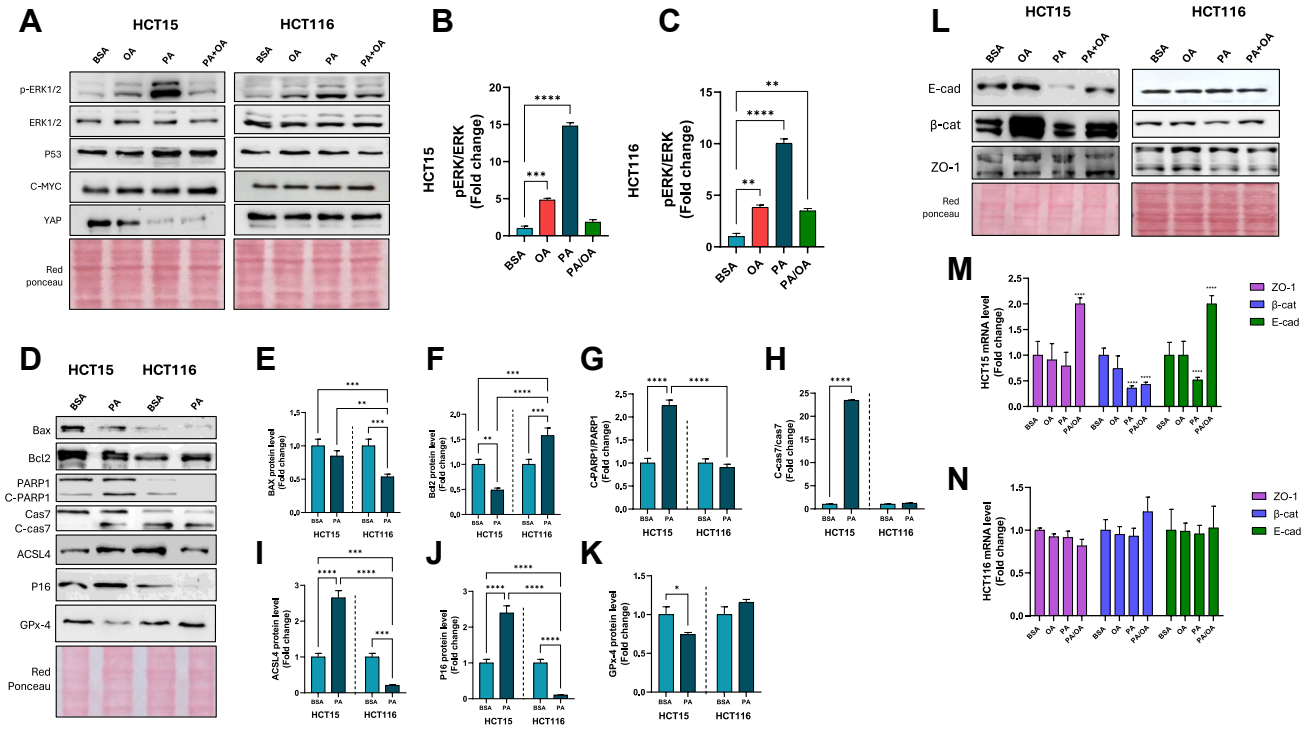

FIG. 4. **Cell signaling, tight junctions, and cell death programs in HCT15 and HCT116 cells.** *A*, representative Western blot analysis of pERK1/2, total ERK1/2, P53, c-Myc, and YAP in HCT15 and HCT116 cells after 24 h of treatment with BSA (control), OA (200 μM), PA (200 μM), or PA + OA (1:1 ratio, 200 μM each). Quantification of pERK/ERK ratios in (*B*) HCT15 and (*C*) HCT116. *D*, Western blot analysis of apoptosis-related markers (Bax, Bcl2, PARP1, cleaved PARP1 [C-PARP1], caspase 7 [Cas7], cleaved caspase 7 [C-Cas7]), ACSL4, p16, and GPx4, and (*E–K*) relative quantifications, including C-PARP1/total PARP1 and C-Cas7/total Cas7 ratios in both cell lines treated with BSA or PA. *L*, representative Western blot analysis of tight junction proteins E-cadherin (E-cad), β-catenin (β-cat), and ZO-1 in HCT15 and HCT116 cells. *M and N*, relative mRNA expression levels of ZO-1, β-cat, and E-cad in HCT15 and HCT116 cells after 24 h of treatment with BSA, OA, PA, or PA + OA. Values represent the mean ± SD of at least three independent experiments. (*$p < 0.05$; **$p < 0.01$; ***$p < 0.005$; ****$p < 0.001$).

with only negligible perturbations in junctional marker expression under identical conditions (Fig. 4, *L–N*).

Palmitic Acid Reprogram Energy Metabolism in Colon Cancer Cells

Among differentially expressed proteins in the two colorectal cancers following PA treatment, we identify many mitochondrial proteins (Supplementary Table S7). To elucidate the impact of fatty acid exposure on mitochondrial functionality, we performed comprehensive bioenergetic profiling using Seahorse XF technology and OXPHOS complex analysis in HCT15 and HCT116 intestinal cells (Fig. 5).

HCT15 cells demonstrated marked metabolic vulnerability to PA treatment, exhibiting a dramatic suppression of both basal and ATP-linked mitochondrial respiration (Fig. 5*A* and *B*) that persisted throughout the measurement period. This respiratory impairment was accompanied by a reduction in extracellular acidification (Fig. 5*A*), indicating no compensatory shift toward glycolytic metabolism. These last data are also confirmed by a significant reduction in glycolysis and glycolytic reserve in PA-treated HCT15 cells (Fig. 5*B*). Proteomics analysis of PA-treated HCT15 cells further supports OCR data, indicating downregulation of proteins involved in mitochondrial oxidative phosphorylation and dynamics (NDUFAF1, NDUFA3, NDUFA10, SURF1, OXA1L, COX20, MFN2, NDUFS3, ATPAF1, ACAD9, LONP1, and YME1L1) (Supplementary Table S7). In striking contrast, OA treatment maintained near-normal respiratory capacity, suggesting preservation of mitochondrial function.

HCT116 cells showed remarkable metabolic resilience across PA treatments (Fig. 5, *F–J*). PA treatments resulted in only modest alterations in basal respiration and ATP-linked mitochondrial respiration, with minimal impact on extracellular acidification rates, glycolysis, and glycolytic reserve (Fig. 5*G*), indicating maintained oxidative capacity and metabolic flexibility. OA treatment in HCT116 cells increased mitochondrial basal respiration and ATP-linked respiration, with a minimal increase also in glycolysis (Fig. 5*G*).

Western blot analysis of OXPHOS subunit complexes provided mechanistic insights into the observed respiratory defects. In HCT15 cells, PA treatment induced significant downregulation of CI (NDUFB8 subunit) and CII (SDHB subunit)

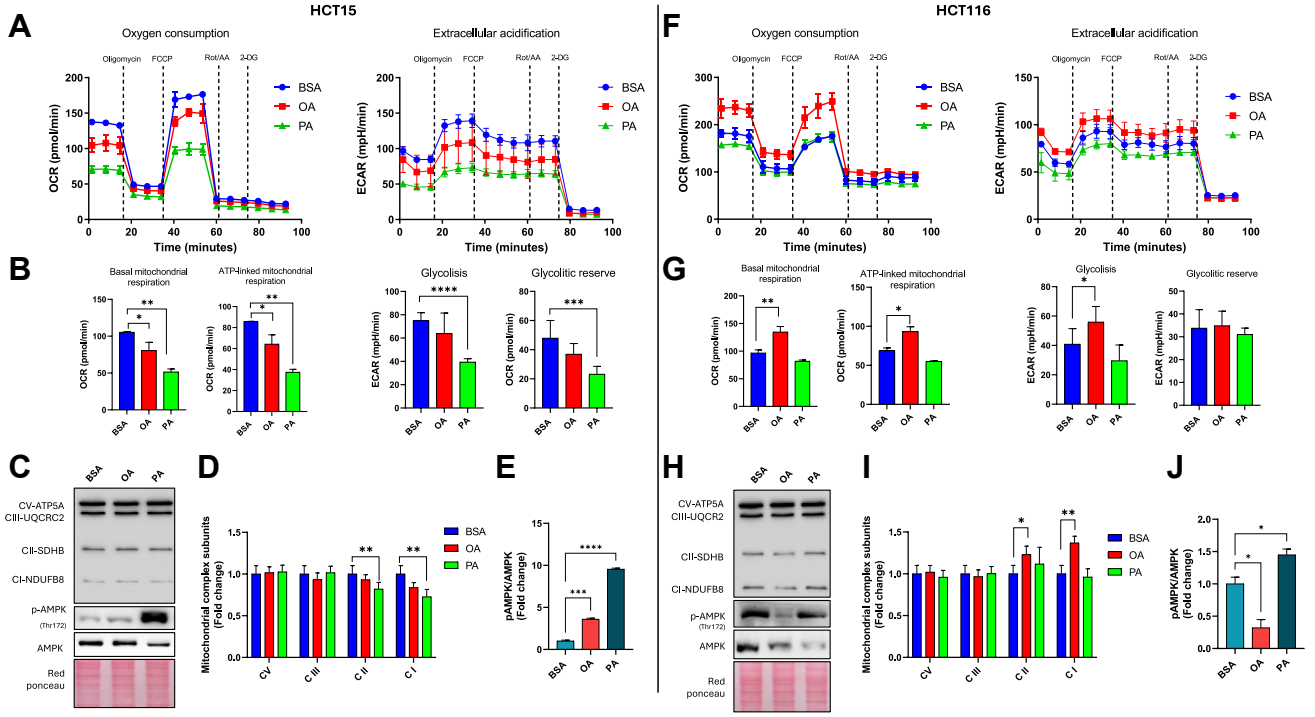

FIG. 5. **Energy metabolism in HCT15 and HCT116 cells.** *A, F*, oxygen consumption rate (OCR) and extracellular acidification rate (ECAR) profiles were assessed using a Seahorse XFp Analyzer in HCT15 and HCT116 cells after 24 h of treatment with BSA (control), OA (200 μM), or PA (200 μM). *B and G*, bioenergetic parameters, including basal respiration, ATP-linked respiration, glycolysis, and glycolytic reserve, were derived from OCR/ECAR curves. Representative Western blot analysis of total OXPHOS, phosphorylated AMPK (p-AMPK, Thr172), and total AMPK in (*C* and *D*) HCT15 and (*H* and *I*) HCT116 cells, with relative quantification of mitochondrial complex subunits (*E*) HCT15 and (*J*) HCT116 p-AMP/AMPK ratioratios. Ponceau S staining was used as a total protein loading control. Values represent the mean ± SD of at least three independent experiments. (*$p < 0.05$; **$p < 0.01$; ***$p < 0.005$; ****$p < 0.001$).

(Fig. 5, *C* and *D*). HCT116 cells showed minimal changes in OXPHOS complex expression, with a trend toward an increase in CII expression (Fig. 5, *H* and *I*). Coherent with the higher basal respiration of HCT116 cells under OA treatment, both CI and CII were upregulated by OA in HCT116 cells (Fig. 5, *H* and *I*).

AMPK, a crucial nutrient and energy sensor, plays a central role in maintaining cellular energy homeostasis (34). Our data revealed that PA treatment led to a marked increase in the phosphorylation of AMPK (p-AMPK) relative to total AMPK levels in both cell lines (Fig. 5, *C*, *E*, *H,* and *J*). Differently, OA treatment did not significantly affect AMPK activation in HCT116 cells, while it enhanced AMPK phosphorylation in HCT15 cells. Importantly, co-treatment with OA did not counteract the PA-induced phosphorylation of AMPK, suggesting that PA triggers a persistent activation of the AMPK pathway independent of OA (data not shown).

EMT Enhances Resistance to Palmitic Acid-Induced Lipotoxicity in HCT15 cells

To further dissect whether the differential sensitivity of HCT15 and HCT116 colorectal cancer cells to the lipotoxic effects of PA could be mechanistically linked to EMT, we assessed the impact of PA in the presence of PMA, a well-characterized EMT inducer (Fig. 6*A*) (35). At the molecular level, PMA treatment induced clear EMT-related changes in HCT15 cells, as reflected by downregulation of the epithelial marker E-cadherin and modulation of key signaling molecules (Fig. 6*B*). Specifically, PMA reduced PKCα and p53 expression while markedly increasing NDRG1 levels in both cell lines, a signature consistent with a shift toward a mesenchymal-like phenotype (32, 33). Phase-contrast microscopy revealed that PA alone elicited profound stress responses in HCT15 cells, manifested by cell rounding and detachment (Supplementary Fig. S4). Remarkably, co-treatment with PMA attenuated these cytotoxic features, preserving cell morphology and suggesting that EMT activation exerts a protective role against PA-induced lipotoxic stress. In sharp contrast, HCT116 cells exhibited only minimal morphological alterations across all treatment conditions, highlighting their intrinsic resistance to PA cytotoxicity (Supplementary Fig. S4).

Cell viability assays further substantiated these observations: in HCT15 cells, PA markedly reduced survival at 24 h,

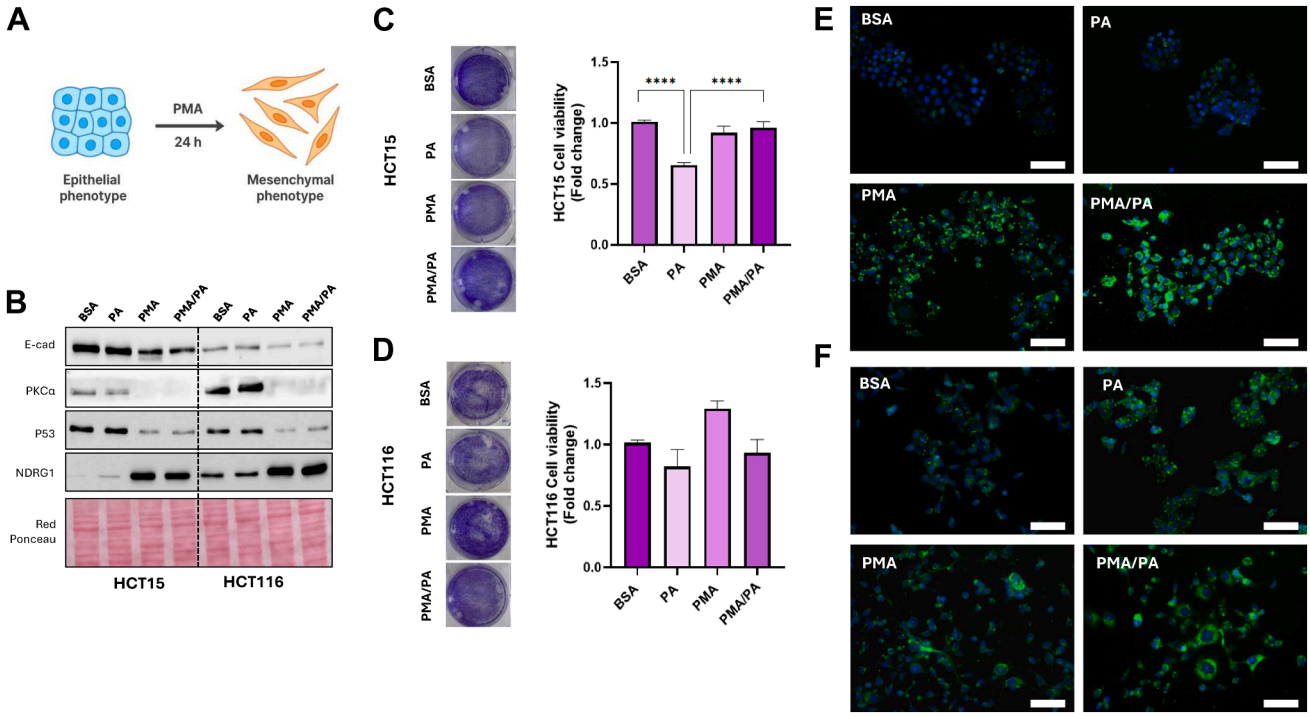

FIG. 6. **EMT confers resistance to palmitic acid-induced lipotoxicity in HCT15 cells.** *A*, schematic illustration (Created with BioRender.com) of the effect of phorbol 12-myristate 13-acetate (PMA) in inducing epithelial–mesenchymal transition (EMT). *B*, representative Western blot analysis of EMT markers (Zeb1, E-cadherin, PKCα, P53, and NDRG1) in HCT15 and HCT116 cells treated for 24 h with BSA (control), PA (200 μM), PMA (100 nM), or PMA + PA. Ponceau S staining was used as a loading control. *C and D*, cell viability assessed by the Crystal Violet assay in HCT15 (*C*) and HCT116 (*D*) cells under the same conditions. *E and F*, representative BODIPY staining images showing lipid droplets accumulation (green) in PMA/PA-treated HCT15 (E) and HCT116 (F) cells. Scale bars: 100 μm. Values are expressed as mean ± SD of at least three independent experiments. (*$p < 0.05$; **$p < 0.01$; ***$p < 0.005$; ****$p < 0.001$).

an effect that was almost completely reversed by PMA co-treatment (Fig. 6*C*). Conversely, in HCT116 cells, neither PA nor PMA significantly impacted viability (Fig. 6*D*). Such remodeling underscores the capacity of EMT to enhance cell survival under metabolic stress conditions.

Notably, LD accumulation was markedly enhanced in HCT15 cells exposed to the PA-PMA combination compared to PA alone, while no such effect was evident in HCT116 cells (Fig. 6, *E* and *F*). Given that LD biogenesis represents a well-established adaptive mechanism to buffer FFA-induced lipotoxicity in hepatocytes (36, 37), our data strongly suggest that PMA-induced EMT promotes LD accumulation as a cytoprotective strategy in HCT15 cells.

Collectively, these findings support the hypothesis that EMT activation by PMA confers a protective advantage against PA-induced lipotoxicity, particularly in HCT15 cells, by driving a mesenchymal-like phenotype associated with enhanced LDs synthesis and activation of pro-survival pathways.

DISCUSSION

Our findings reveal a fundamental relationship between EMT status and cellular vulnerability to saturated fatty acid-induced stress in colorectal cancer. The striking differential sensitivity of HCT15 and HCT116 cells to PA extends beyond simple cytotoxicity, encompassing divergent metabolic reprogramming, lipid handling capacity, and activation of distinct cell death pathways. These observations align with emerging evidence that EMT confers broad metabolic plasticity and stress resistance in cancer cells (32, 38), but our study uniquely demonstrates how this phenotypic state specifically modulates responses to dietary lipid exposure.

We acknowledge that the present study focuses on two colorectal cancer cell lines with distinct baseline phenotypes (HCT15, predominantly epithelial-like; HCT116, more mesenchymal-like). This design was chosen to contrast two extreme states and to uncover mechanistic links between EMT features and lipid stress responses; however, it does not capture the full molecular heterogeneity of colorectal cancer. Therefore, we have tempered statements of generalization throughout the manuscript and frame our conclusions as applying to these models. Future work should validate the key observations (differential LD storage capacity, DGAT regulation, and lipotoxic sensitivity) in additional epithelial and mesenchymal CRC models and in patient-derived organoids, ideally including isogenic systems to disentangle EMT status from genetic background (e.g., TP53).

The mesenchymal-like phenotype of HCT116 cells, characterized by elevated Zeb-1, PKCα, and NDRG1 expression alongside reduced E-cadherin, appears to establish a pre-adapted metabolic state capable of buffering lipotoxic stress. This interpretation is consistent with recent work demonstrating that mesenchymal cancer cells exhibit enhanced metabolic flexibility and can efficiently redirect excess nutrients toward biosynthetic pathways rather than toxic accumulation (39). Conversely, the epithelial characteristics of HCT15 cells, robust cell-cell junctions, high E-cadherin expression, and organized polarity, may paradoxically render these cells more vulnerable to membrane lipid perturbations that disrupt cellular architecture.

The inability of HCT15 cells to accumulate LDs in response to PA represents a critical metabolic failure that likely drives their enhanced sensitivity to lipotoxicity. Our observation that PA downregulates the expression of DGAT1 and DGAT2 specifically in HCT15 cells provides a molecular mechanism for this deficiency. These findings resonate strongly with recent studies in hepatocytes demonstrating that DGAT1 downregulation under PA exposure compromises the cell capacity to sequester toxic FFA into neutral lipid stores (10). The concept of LDs as "metabolic buffers" that protect cells from lipotoxicity is well established in liver biology (36, 37), and our data extend this paradigm to colorectal cancer cells, suggesting that LD biogenesis capacity fundamentally determines cellular fate under lipid stress.

The proteomic identification of elevated PLIN2 expression in HCT116 cells following PA treatment supports this interpretation, as PLIN2 is a key structural protein that stabilizes nascent LDs and prevents their premature lipolysis (40). The coordinated upregulation of both PLIN2 and maintained DGAT expression in HCT116 cells likely creates a permissive environment for lipid storage that is absent in HCT15 cells.

Our observation that PA induces simultaneous activation of apoptotic markers and ferroptosis signatures in HCT15 cells challenges traditional views of cell death as discrete, mutually exclusive pathways. The constellation of findings, ACSL4 upregulation, GPx4 downregulation, iron metabolism dysregulation, alongside PARP-1 cleavage, caspase-7 activation, and Bcl-2 suppression, strongly suggests a hybrid ferroptosis-apoptosis mechanism. This interpretation aligns with emerging evidence that cells under metabolic stress can activate multiple death pathways simultaneously, with the outcome representing the integrated effect of these signals (41).

ACSL4 has a central role in incorporating polyunsaturated fatty acids into membrane phospholipids, making it a critical determinant of ferroptosis susceptibility. Its selective upregulation in PA-treated HCT15 cells, coupled with GPx4 downregulation, creates a highly permissive context for lipid peroxidation-driven damage. Unlike apoptosis, ferroptosis is not caspase-dependent but rather relies on oxidative and lipid imbalance, and our model supports this hypothesis. In contrast, HCT116 cells, thanks to their enhanced metabolic plasticity and efficient lipid storage, appear less susceptible to ferroptosis. This is particularly relevant given that saturated fatty acids like PA can promote conditions favoring ferroptosis in cells with impaired antioxidant defenses and compromised lipid storage (42). The proteomic identification of coordinated upregulation of ferroptosis-related proteins, SLC7A11, HMOX1, SESN2, SQSTM1/p62, and CAT, further supports the activation of this pathway.

The possible engagement of ferroptosis and apoptotic machinery might reflect the severity of metabolic disruption in PA-treated HCT15 cells. Classical apoptosis typically requires ATP and functional mitochondria, yet our bioenergetic profiling revealed catastrophic metabolic failure in these cells. Under such conditions, alternative ATP-independent death pathways like ferroptosis may become increasingly important. The hybrid nature of cell death in this context may thus represent not redundancy but rather complementary mechanisms ensuring elimination of severely compromised cells.

The comprehensive bioenergetic failure observed in PA-treated HCT15 cells, characterized by suppressed mitochondrial respiration and impaired glycolytic capacity, reveals that lipotoxicity extends far beyond simple membrane perturbation. The proteomic evidence of downregulated OXPHOS complex proteins (NDUFA, SURF1, and OXA1L) and mitochondrial dynamics regulators (MFN2, LONP1, and YME1L1) suggests that PA actively dismantles mitochondrial infrastructure in susceptible cells. This interpretation differs from models proposing simple substrate overload and instead suggests active suppression of mitochondrial biogenesis or accelerated mitochondrial degradation.

The inability of HCT15 cells to compensate for respiratory failure by upregulating glycolysis represents a particularly striking metabolic inflexibility. In contrast, cancer cells typically exhibit remarkable metabolic plasticity, readily switching between oxidative phosphorylation and glycolysis depending on substrate availability and oxygen tension (the Warburg effect). The loss of this flexibility in PA-treated HCT15 cells may reflect either direct glycolytic enzyme inhibition or broader disruption of metabolic regulatory networks. The reduction in both glycolysis and glycolytic reserve suggests fundamental impairment of glucose metabolism.

The metabolic resilience of HCT116 cells, maintaining near-normal respiratory and glycolytic capacity despite PA exposure, likely contributes significantly to their survival advantage. Their ability to even increase mitochondrial respiration under OA treatment demonstrates intact metabolic machinery capable of adapting to lipid substrate availability. This metabolic competence may stem from their mesenchymal phenotype, which has been associated with enhanced mitochondrial function and oxidative metabolism in multiple cancer contexts (43).

These metabolic distinctions may, at least in part, derive from differences in p53 functionality between the two cell

lines. Beyond its established roles in cell cycle arrest and apoptosis, p53 is a central regulator of cellular metabolism. Wild-type p53 supports mitochondrial oxidative phosphorylation, maintains mitochondrial integrity, and suppresses excessive glycolytic activity, thereby ensuring an efficient and balanced bioenergetic state (44). Conversely, loss or dysfunction of p53 disrupts this homeostasis, leading to impaired mitochondrial respiration and a compensatory shift toward glycolysis, a hallmark of metabolic rewiring consistently demonstrated in both cultured cells and *in vivo* models. In this context, the proteomic differences observed between HCT116 (p53 wild type) and HCT15 (p53 mutant) are consistent with their distinct metabolic phenotypes and reinforce the concept that p53 status shapes both metabolic and phenotypic traits in colorectal cancer cells.

The higher baseline expression of PKCα and NDRG1 in HCT116 cells, and their further modulation by PMA-induced EMT in HCT15 cells, points to these proteins as potential mediators of lipotoxic resistance. The well-established roles of PKCα in regulating TJ dynamics and cell survival signaling (45, 46) position it as a key effector in maintaining barrier function under stress. Its activation may promote cytoskeletal remodeling that stabilizes membrane integrity during lipid challenges, while simultaneously activating pro-survival pathways that counteract apoptotic signals.

The context-dependent functions of NDRG1 in cancer make it a particularly intriguing player. While traditionally viewed as a metastasis suppressor, recent evidence demonstrates that NDRG1 can promote survival and stress tolerance in mesenchymal-like tumor cells (47, 48). Our observation that NDRG1 is elevated in resistant HCT116 cells and further induced by EMT-promoting PMA treatment in HCT15 cells suggests it functions as an adaptive stress response protein in this context. The ability of NDRG1 to modulate cellular iron homeostasis may be particularly relevant given the ferroptosis component of PA-induced cell death, as proper iron regulation is critical for preventing Fenton reaction-driven lipid peroxidation.

Notably, *MYC* expression exhibited variable regulation, reflecting its well-documented context-dependent duality: while promoting proliferation under physiological conditions, c-Myc paradoxically sensitizes cells to apoptosis during stress scenarios characterized by ERK hyperactivation or YAP suppression (49). The simultaneous activation of these stress-responsive pathways suggests that PA triggers a coordinated cellular response that ultimately favors cell death over survival.

The selective disruption of E-cadherin, β-catenin, and ZO-1 expression in PA-treated HCT15 cells reveals that saturated fatty acid exposure can trigger EMT-like changes that compromise epithelial architecture. This observation extends previous findings that PA disrupts intestinal barrier integrity (15) by demonstrating that the effect is cell phenotype dependent. The rescue of junctional protein expression by OA co-treatment is particularly noteworthy, suggesting that unsaturated fatty acids may actively stabilize epithelial architecture through mechanisms beyond the simple absence of saturated fatty acid toxicity.

The relationship between junctional disruption and lipotoxic sensitivity remains incompletely understood. Loss of E-cadherin-mediated adhesion could potentially sensitize cells to membrane stress by eliminating cooperative survival signaling between adjacent cells. Alternatively, E-cadherin downregulation may be a consequence rather than a cause of cellular stress, reflecting activation of EMT-inducing transcription factors downstream of lipotoxic signals. The fact that forced EMT induction protects HCT15 cells from PA toxicity argues that phenotypic transition itself, with its attendant metabolic reprogramming, confers the protective effect, rather than simply the presence or absence of specific junctional proteins.

The protective effect of PMA-induced EMT in HCT15 cells provides compelling causal evidence that mesenchymal transition enhances lipotoxic resistance. PMA treatment not only attenuated PA-induced cytotoxicity but also enhanced LDs accumulation, suggesting that EMT coordinately reprograms multiple aspects of lipid metabolism. This observation aligns with emerging evidence that EMT involves comprehensive metabolic rewiring, including enhanced fatty acid oxidation, altered lipid synthesis pathways, and modified mitochondrial function (50).

It is important to note, however, that PMA is a potent pharmacological activator of PKC with pleiotropic and potentially cell line-dependent effects, and it may not fully recapitulate physiological EMT cues present in the tumor microenvironment. In this study, we used PMA as an established experimental tool to transiently shift EMT-associated markers and to probe causality between EMT-linked reprogramming and resistance to lipotoxicity. Future studies should validate the EMT-lipotoxicity relationship using additional EMT induction models (e.g., TGF-β-driven EMT) and genetic approaches (e.g., modulation of ZEB1/SNAI1 or PKCα signaling) across a broader panel of colorectal cancer models.

The molecular changes induced by PMA, E-cadherin downregulation, PKCα and p53 suppression, NDRG1 upregulation, partially recapitulate the baseline phenotype of HCT116 cells, supporting the interpretation that these markers define a stress-resistant cellular state. Interestingly, the ability of PMA to reduce p53 expression may contribute to its protective effect, as p53 stabilization was identified as a key mediator of PA-induced death in untreated HCT15 cells. This suggests that mesenchymal cells may evade lipotoxicity partly through attenuated p53 responses, allowing them to tolerate metabolic stress that would trigger apoptosis in epithelial cells.

Our findings have several potential clinical implications for understanding how dietary fat composition influences

colorectal cancer progression and treatment responses. The observation that mesenchymal-like cancer cells resist saturated fatty acid-induced stress suggests that dietary interventions targeting lipid composition might differentially affect tumors based on their EMT status. Epithelial-like tumors might be particularly vulnerable to saturated fat-mediated cytotoxicity, while mesenchymal tumors could potentially thrive under high saturated fat conditions.

Colorectal cancers display substantial inter- and intra-tumor heterogeneity, and EMT-like transcriptional programs are frequently enriched in advanced disease and metastatic lesions. Metastatic dissemination, particularly to the liver, occurs in a lipid-rich environment in which circulating albumin-bound FFAs and local lipid stores are abundant. In this context, enhanced neutral-lipid storage and LD buffering could plausibly support tumor cell survival during detachment, circulation and colonization by limiting acute lipotoxic stress. Our *in vitro* data are consistent with such a model: the more mesenchymal-like HCT116 cells maintain DGAT expression and induce PLIN2-positive LDs in response to PA, whereas the epithelial-like HCT15 cells fail to mount this protective storage response and undergo cell death.

In line with the emerging view that LD buffering capacity shapes cellular responses to saturated fatty acids, Zhao *et al*. recently reported that PA increased LD formation and modulated tumor cell phenotypes in another cancer context, and that pharmacological depletion of LDs by DGAT1/DGAT2 inhibition sensitized cells to PA-induced stress (51). Although performed in a different tumor type, these observations support the broader concept highlighted by our study: the capacity to sequester lipids into LDs is a key determinant of whether saturated fatty acids act as a metabolic substrate or a cytotoxic insult.

The identification of ferroptosis as a component of lipotoxic cell death opens potential therapeutic avenues. Ferroptosis-inducing agents are being explored as cancer therapeutics (52), and our data suggest that combining such agents with dietary or pharmacological strategies that promote saturated fatty acid exposure might synergistically eliminate epithelial cancer cells while sparing normal tissues. Conversely, inhibiting EMT in mesenchymal tumors might sensitize them to lipotoxic stress.

The protective effect of OA co-treatment observed throughout our study suggests that dietary fat quality, not just quantity, critically influences cancer cell fate. This aligns with epidemiological evidence associating Mediterranean diets, rich in monounsaturated fats from olive oil, with reduced colorectal cancer risk (53). Our mechanistic data provide cellular and molecular support for these epidemiological observations.

While our study provides comprehensive characterization of differential lipotoxic responses in EMT-distinct colorectal cancer cell lines, several questions remain. First, the *in vivo* relevance of the proposed EMT-lipid-buffering axis requires validation in animal models of primary and metastatic colorectal cancer as well as in human tumor samples. Second, because our conclusions are based on 2 cell lines with distinct genetic backgrounds, we cannot exclude contributions from cell line-specific alterations (including TP53 status) to some of the observed phenotypes. Future work using additional epithelial and mesenchymal colon rectal cancer cells, patient-derived organoids and/or isogenic systems will be important to disentangle EMT state from genetic background. Finally, although PMA provided a convenient tool to perturb EMT-associated markers, complementary approaches using more physiological EMT stimuli and genetic modulation will strengthen causal inference.

CONCLUSION

From a broader perspective, these findings position EMT not only as a driver of invasiveness and metastasis but also as a fundamental determinant of metabolic fate under nutrient or lipid stress. The proteomic evidence supports the view that EMT confers a “metabolic armor,” reorganizing mitochondrial and lipid-handling systems to sustain cell viability even in the presence of potentially cytotoxic fatty acids. Such metabolic plasticity may explain why mesenchymal-like tumors exhibit greater survival and therapeutic resistance in lipid-rich microenvironments, a scenario increasingly relevant in obesity-associated cancers.

Altogether, the comparative proteomic analysis of HCT15 and HCT116 cells reveals that EMT rewires the proteome in a manner that integrates structural, metabolic, and stress-response functions. This reprogramming transforms how cells perceive and manage lipid challenges, turning palmitic acid from a lethal insult in epithelial contexts into a manageable metabolic substrate in mesenchymal ones. Understanding this proteomic shift opens new avenues for targeting EMT-associated metabolic adaptations, potentially exploiting lipotoxic stress as a therapeutic vulnerability in epithelial-like colorectal cancers.

DATA AVAILABILITY

The data are available from the corresponding author upon reasonable request.

The mass spectrometry proteomics data generated in this study have been deposited to the ProteomeXchange Consortium via the PRIDE partner repository with the dataset identifier PXD071641. During peer review, the dataset can be accessed by the reviewers using the following credentials: Processed DIA-NN output tables and the complete protein quantification matrix (Supplementary Table 8) are provided as part of the PRIDE submission.

Direct reviewer login: Username: reviewer_pxd071641@ebi.ac.uk; Password: IaYMt09wy6fW.

Via project token access: Project accession: PXD071641; Token: I70vbcRp133O.

Supplemental data—This article contains supplemental data.

Acknowledgments—We acknowledge support from the IDENTITA project (T5-AN-01), "Integrated Mediterranean Network for Personalized Nutrition Pathways against Malnutrition," coordinated by the Puglia Region – Health Marketplace. We also gratefully acknowledge the "Plateformes Lilloises en Biologie et Santé (PLBS) – UAR 2014 – US 41" for providing access to the imaging facility. The mass spectrometry proteomics data have been deposited to the ProteomeXchange Consortium via the PRIDE (54) partner repository with the dataset identifier PXD071641.

Author Contributions—A. M. G., D. V., F. V., I. S., E. B., and E. S. supervision; A. M. G., D. V., F. V., I. S., E. B., and E. S. writing–original draft; A. M. G., D. V., F. V., I. S., E. B., and E. S. conceptualization; I. S., F. V., and E. B. investigation; I. S., F. V., and E. B. methodology; I. S., F. V., and E. B. validation; F. V., S. M., A. R., and Y. Z. software; F.V., S. M., A. R., and Y. Z. formal analysis; S. M., A. R., and Y. Z. data curation; M. S., I. F., and A. M. G. funding acquisition; M. S., I. F., and A. M. G. project administration; M. S., I. F., and A. M. G. resources; M. S., I. F., and A. M. G. investigation.

Funding and additional information—This work is partially supported by the Institut National de la Santé et de la Recherche Biomédicale, Région Hauts de France, Université de Lille, Agence Nationale de la recherche (Click & Detect, CE29, 2024), CPER Resistomics, and CPER Tech-Santé. The authors thank the OrganOmics platform of PRISM Inserm U1192, which is recognized and supported by the University of Lille, the Infrastructure PROFI (https://www.profiproteomics.fr/), and the GIS IbiSA (https://www.ibisa.net/). The OrganOmics platform (Villeneuve d'Ascq, France) is also supported by Region Hauts de France and FEDER funding.

Conflict of interest—The authors declare that they do not have any conflicts of interest with the content of this article.

Abbreviations—The abbreviations used are: AANOVA, analysis of variance; ACSL4, acyl-CoA synthetase long chain family member 4; BCA, bicinchoninic acid; DGAT, diacylglycerol O-acyltransferases; ECAR, extracellular acidification rate; EMT, epithelial–mesenchymal transition; ER, endoplasmic reticulum; FA, formic acid; FASP, filter-aided sample preparation; FDR, false discovery rate; FFAs, free fatty acids; GAPDH, Glyceraldehyde-3-phosphate dehydrogenase; HFD, high-fat diet; TAG, triacylglycerol; LDs, lipid droplets; OA, oleic acid; PA, palmitic acid; PBS, phosphate-buffered saline; TBS, Tris-buffered saline; TFA, trifluoroacetic acid; TLC, Thin-Layer Chromatography; UPR, unfolded protein response.

Received December 9, 2025, and in revised form, February 11, 2026 Published, MCPRO Papers in Press, March 12, 2026, https://doi.org/10.1016/j.mcpro.2026.101554

REFERENCES

1. Khonsary, S. (2017) Guyton and hall: textbook of medical physiology. *Surg. Neurol. Int.* **8**, 275
2. Honey, K. (2006) DC family welcomes a new arrival. *Nat. Rev. Immunol.* **6**, 172
3. Nelson, W. J., and Nusse, R. (2004) Convergence of wnt, ß-Catenin, and cadherin pathways. *Science (1979)* **303**, 1483–1487
4. Lindley, D. (2001) Falling to Earth in a quantum way. *Nature* **410**, 145–146
5. Sánchez-Tilló, E., de Barrios, O., Siles, L., Cuatrecasas, M., Castells, A., and Postigo, A. (2011) β-catenin/TCF4 complex induces the epithelial-to-mesenchymal transition (EMT)-activator ZEB1 to regulate tumor invasiveness. *Proc. Natl. Acad. Sci. U. S. A.* **108**, 19204–19209
6. Xu, Y., Liu, L., Xin, W., Zhao, X., Chen, L., Zhen, J., *et al*. (2015) The renoprotective role of autophagy activation in proximal tubular epithelial cells in diabetic nephropathy. *J. Diabetes Complications* **29**, 976–983
7. Perler, B. K., Friedman, E. S., and Wu, G. D. (2023) The role of the gut Microbiota in the relationship between diet and human health. *Annu. Rev. Physiol.* **85**, 449–468
8. Rizzo, W. B., Craft, D. A., Somer, T., Carney, G., Trafrova, J., and Simon, M. (2008) Abnormal fatty alcohol metabolism in cultured keratinocytes from patients with Sjögren-Larsson syndrome. *J. Lipid Res.* **49**, 410–419
9. Schröder, M., and Kaufman, R. J. (2005) The MAMMALIAN UNFOLDED PROTEIN RESPONSE. *Annu. Rev. Biochem.* **74**, 739–789
10. Moliterni, C., Vari, F., Schifano, E., Tacconi, S., Stanca, E., Friuli, M., *et al*. (2024) Lipotoxicity of palmitic acid is associated with DGAT1 down-regulation and abolished by PPARα activation in liver cells. *J. Lipid Res.* **65**, 100692
11. Pinçon, A., Coulombe, J.-D., Chouinard-Watkins, R., and Plourde, M. (2016) Human apolipoprotein E allele and docosahexaenoic acid intake modulate peripheral cholesterol homeostasis in mice. *J. Nutr. Biochem.* **34**, 83–88
12. Kim, C., Hong, Y., Lee, H., Kang, H., and Lee, E. K. (2018) MicroRNA-195 desensitizes HCT116 human colon cancer cells to 5-fluorouracil. *Cancer Lett.* **412**, 264–271
13. Romani, A., Ieri, F., Urciuoli, S., Noce, A., Marrone, G., Nediani, C., *et al*. (2019) Health effects of phenolic compounds found in extra-virgin olive oil, By-Products, and leaf of Olea europaea L. *Nutrients* **11**, 1776
14. Achamrah, N., Coëffier, M., and Déchelotte, P. (2016) Physical activity in patients with anorexia nervosa. *Nutr. Rev.* **74**, 301–311
15. Stolfi, C., Maresca, C., Monteleone, G., and Laudisi, F. (2022) Implication of intestinal barrier dysfunction in gut dysbiosis and diseases. *Biomedicines* **10**, 289
16. Stockwell, B. R., Jiang, X., and Gu, W. (2020) Emerging mechanisms and disease relevance of ferroptosis. *Trends Cell Biol.* **30**, 478–490
17. Sun, D., Wang, L., Wu, Y., Yu, Y., Yao, Y., Yang, H., *et al*. (2025) Lipid metabolism in ferroptosis: mechanistic insights and therapeutic potential. *Front Immunol.* **16**. https://doi.org/10.3389/fimmu.2025.1545339
18. Knutsen, T., Padilla-Nash, H. M., Wangsa, D., Barenboim-Stapleton, L., Camps, J., McNeil, N., *et al*. (2010) Definitive molecular cytogenetic characterization of 15 colorectal cancer cell lines. *Genes Chromosomes Cancer* **49**, 204–223
19. Sánchez-Martínez, R., Cruz-Gil, S., de Cedrón, M. G., Álvarez-Fernández, M., Vargas, T., Molina, S., *et al*. (2015) A link between lipid metabolism and epithelial-mesenchymal transition provides a target for colon cancer therapy. *Oncotarget* **6**, 38719–38736
20. Monti, P., Ravera, S., Speciale, A., Velkova, I., Foggetti, G., Degan, P., *et al*. (2022) Mutant p53K120R expression enables a partial capacity to modulate metabolism. *Front Genet.* **13**. https://doi.org/10.3389/fgene.2022.974662
21. Carta, G., Murru, E., Banni, S., and Manca, C. (2017) Palmitic acid: physiological role, metabolism and nutritional implications. *Front Physiol.* **8**. https://doi.org/10.3389/fphys.2017.00902

22. Palomino, O., Giordani, V., Chowen, J., Alfonso, S. F., and Goya, L. (2022) Physiological doses of oleic and palmitic acids protect human endothelial cells from oxidative stress. *Molecules* **27**, 5217
23. Domínguez-López, I., Arancibia-Riveros, C., Casas, R., Tresserra-Rimbau, A., Razquin, C., Martínez-González, M.Á., *et al*. (2022) Changes in plasma total saturated fatty acids and palmitic acid are related to pro-inflammatory molecule IL-6 concentrations after nutritional intervention for one year. *Biomed. Pharmacother.* **150**, 113028
24. Heberle, H., Meirelles, G. V., da Silva, F. R., Telles, G. P., and Minghim, R. (2015) InteractiVenn: a web-based tool for the analysis of sets through Venn diagrams. *BMC Bioinformatics* **16**, 169
25. Zirem, Y., Ledoux, L., Fournier, I., and Salzet, M. (2025) Profiler: an open web platform for multi-omics analysis. *Bioinformatics*. , btaf644. https://doi.org/10.1093/bioinformatics/btaf644
26. Szklarczyk, D., Kirsch, R., Koutrouli, M., Nastou, K., Mehryary, F., Hachilif, R., *et al*. (2023) The STRING database in 2023: protein–protein association networks and functional enrichment analyses for any sequenced genome of interest. *Nucleic Acids Res.* **51**, D638–D646
27. Matyash, V., Liebisch, G., Kurzchalia, T. V., Shevchenko, A., and Schwudke, D. (2008) Lipid extraction by methyl-tert-butyl ether for high-throughput lipidomics. *J. Lipid Res.* **49**, 1137–1146
28. Giudetti, A. M., Guerra, F., Longo, S., Beli, R., Romano, R., Manganelli, F., *et al*. (2020) An altered lipid metabolism characterizes charcot-marie-tooth type 2B peripheral neuropathy. *Biochim. Biophys. Acta (Bba) - Mol. Cell Biol. Lipids* **1865**, 158805
29. Uhlén, M., Fagerberg, L., Hallström, B. M., Lindskog, C., Oksvold, P., Mardinoglu, A., *et al*. (2015) Tissue-based map of the human proteome. *Science (1979)* **347**. https://doi.org/10.1126/science.1260419
30. Fernández, L. P., Gómez de Cedrón, M., and Ramírez de Molina, A. (2020) Alterations of lipid metabolism in cancer: implications in prognosis and treatment. *Front Oncol.* **10**. https://doi.org/10.3389/fonc.2020.577420
31. Zhang, W., Liu, Y., Liao, Y., Zhu, C., and Zou, Z. (2024) GPX4, ferroptosis, and diseases. *Biomed. Pharmacother.* **174**, 116512
32. Kalluri, R., and Weinberg, R. A. (2009) The basics of epithelial-mesenchymal transition. *J. Clin. Invest.* **119**, 1420–1428
33. Lamouille, S., Xu, J., and Derynck, R. (2014) Molecular mechanisms of epithelial–mesenchymal transition. *Nat. Rev. Mol. Cell Biol.* **15**, 178–196
34. Jang, M., Park, R., Kim, H., Namkoong, S., Jo, D., Huh, Y. H., *et al*. (2018) AMPK contributes to autophagosome maturation and lysosomal fusion. *Sci. Rep.* **8**, 12637
35. He, H., Davidson, A. J., Wu, D., Marshall, F. F., Chung, L. W. K., Zhau, H. E., *et al*. (2010) Phorbol ester phorbol-12-myristate-13-acetate induces epithelial to mesenchymal transition in human prostate cancer ARCaP E cells. *Prostate* **70**, 1119–1126
36. Listenberger, L. L., Han, X., Lewis, S. E., Cases, S., Farese, R. V., Ory, D. S., *et al*. (2003) Triglyceride accumulation protects against fatty acid-induced lipotoxicity. *Proc. Natl. Acad. Sci. U. S. A.* **100**, 3077–3082
37. Walther, T. C., and Farese, R. V. (2012) Lipid droplets and cellular lipid metabolism. *Annu. Rev. Biochem.* **81**, 687–714
38. Thiery, J. P., Acloque, H., Huang, R. Y. J., and Nieto, M. A. (2009) Epithelial-Mesenchymal transitions in development and disease. *Cell* **139**, 871–890
39. Khan, F., Elsori, D., Verma, M., Pandey, S., Obaidur Rab, S., Siddiqui, S., *et al*. (2024) Unraveling the intricate relationship between lipid metabolism and oncogenic signaling pathways. *Front. Cell Dev. Biol.* **12**. https://doi.org/10.3389/fcell.2024.1399065
40. Wu, Y., Chen, K., Li, L., Hao, Z., Wang, T., Liu, Y., *et al*. (2022) Plin2-mediated lipid droplet mobilization accelerates exit from pluripotency by lipidomic remodeling and histone acetylation. *Cell Death Differ.* **29**, 2316–2331
41. Huang, S., Cao, B., Zhang, J., Feng, Y., Wang, L., Chen, X., *et al*. (2021) Induction of ferroptosis in human nasopharyngeal cancer cells by cucurbitacin B: molecular mechanism and therapeutic potential. *Cell Death Dis.* **12**, 237
42. Feng, S., Tang, D., Wang, Y., Li, X., Bao, H., Tang, C., *et al*. (2023) The mechanism of ferroptosis and its related diseases. *Mol. Biomed.* **4**, 33
43. Jia, D., Park, J., Jung, K., Levine, H., and Kaipparettu, B. A. (2018) Elucidating the metabolic plasticity of cancer: mitochondrial reprogramming and hybrid metabolic States. *Cells* **7**, 21
44. Liang, Y., Liu, J., and Feng, Z. (2013) The regulation of cellular metabolism by tumor suppressor p53. *Cell Biosci.* **3**, 9
45. Le, T. L., Joseph, S. R., Yap, A. S., and Stow, J. L. (2002) Protein kinase C regulates endocytosis and recycling of E-cadherin. *Am. J. Physiol. Cell Physiol.* **283**, C489–C499
46. Andreeva, A. Y., Piontek, J., Blasig, I. E., and Utepbergenov, D. I. (2006) Assembly of tight junction is regulated by the antagonism of conventional and novel protein kinase C isoforms. *Int. J. Biochem. Cell Biol.* **38**, 222–233
47. Li, A., Zhu, X., Wang, C., Yang, S., Qiao, Y., Qiao, R., *et al*. (2019) Upregulation of NDRG1 predicts poor outcome and facilitates disease progression by influencing the EMT process in bladder cancer. *Sci. Rep.* **9**, 5166
48. Saponaro, C., Damato, M., Stanca, E., Aboulouard, S., Zito, F. A., De Summa, S., *et al*. (2024) Unraveling the protein kinase C/NDRG1 signaling network in breast cancer. *Cell Biosci.* **14**, 156
49. Juin, P., Hueber, A.-O., Littlewood, T., and Evan, G. (1999) c-Myc-induced sensitization to apoptosis is mediated through cytochrome c release. *Genes Dev.* **13**, 1367–1381
50. Sciacovelli, M., and Frezza, C. (2017) Metabolic reprogramming and epithelial-to-mesenchymal transition in cancer. *FEBS J.* **284**, 3132–3144
51. Zhao, Z., Wang, J., Kong, W., Newton, M. A., Burkett, W. C., Sun, W., *et al*. (2024) Palmitic acid exerts anti-tumorigenic activities by modulating cellular stress and lipid droplet Formation in endometrial cancer. *Biomolecules* **14**, 601
52. He, Y., Lin, Y., Song, J., Song, M., Nie, X., Sun, H., *et al*. (2025) From mechanisms to medicine: ferroptosis as a Therapeutic target in liver disorders. *Cell Commun. Signal.* **23**, 125
53. Ungvari, Z., Fekete, M., Fekete, J. T., Grosso, G., Ungvari, A., and Győrffy, B. (2024) Adherence to the Mediterranean diet and its protective effects against colorectal cancer: a meta-analysis of 26 studies with 2,217,404 participants. *Geroscience* **47**, 1105–1121
54. Perez-Riverol, Y., Bandla, C., Kundu, D. J., Kamatchinathan, S., Bai, J., Hewapathirana, S., *et al*. (2025) The PRIDE database at 20 years: 2025 update. *Nucleic Acids Res.* **53**, D543–D553